Comprehensive study of band structure driven thermoelectric response of math xmlns="http://www.w3.org/1998/Math/MathML">msub>mi >ZrTe/mi>mn>5/mn>/msub>/math>

Junbo Zhu, Changmin Lee, Fahad Mahmood, Takehito Suzuki, Shiang Fang, Nuh Gedik, and Joseph G. Checkelsky

Phys. Rev. B **106**, 115105 — Published 6 September 2022

DOI: 10.1103/PhysRevB.106.115105

Comprehensive Study of Band Structure Driven Thermoelectric Response of $ZrTe_5$

Junbo Zhu,[1] Changmin Lee,[1,*] Fahad Mahmood,[1,†] Takehito Suzuki,[1,‡] Shiang Fang,[2,1] Nuh Gedik,[1] and Joseph G. Checkelsky[1]

[1] *Department of Physics, Massachusetts Institute of Technology, Cambridge, Massachusetts 02139, USA*
[2] *Department of Physics and Astronomy, Center for Materials Theory, Rutgers University, Piscataway, NJ, USA*

(Dated: August 25, 2022)

We report a transport, thermodynamic, and spectroscopic study of $ZrTe_5$ with a focus on elucidating the connections between its band structure and unusual thermoelectric properties. Using time and angle resolved photoemission spectroscopy (tr-ARPES) we observe a small electronic band gap and temperature dependent Fermi level which traverses from a single valence to conduction band with lowering temperature, consistent with previous reports. This low temperature Fermi surface closely matches that derived from quantum oscillations, suggesting it is reflective of the bulk electronic structure. The Seebeck and low field Nernst response is characterized by an unusually large and non-monotonic temperature evolution. We find this can be quantitatively explained using a semiclassical model based on the observed band character and a linear temperature shifting of the Fermi level. Additionally, we observe a large, non-saturating enhancement of both thermoelectric coefficients in magnetic field. We show this can be captured by the Zeeman energy associated with a large effective g-factor of 25.8 consistent with that derived from Lifshitz-Kosevich analysis of the quantum oscillations. Together these observations provide a comprehensive picture of $ZrTe_5$ as a model high mobility small Fermi surface system and potential platform for significant magnetic field driven thermoelectricity.

I. INTRODUCTION

The layered material $ZrTe_5$ has seen a renewed interest in recent years following the prediction that it could harbor topologically non-trivial ground states [1]. Originally investigated as a potential charge density wave host [2, 3], the system shows a large, sign-changing Seebeck response long interpreted as evidence for a change of dominant carrier type [4]. The nature of this crossover has become of heightened interest, as different theoretical models [1, 5–9] and experiments including ARPES [10–16], Scanning Tunneling Spectroscopy (STS) [12, 13, 17], infrared spectroscopy [18–21], and quantum oscillations [22–26] suggest the system could be a strong topological insulator (TI), weak TI, or Dirac semimetal. At the same time, recent studies have reported a remarkable set of exotic but seemingly disparate phenomena including a chiral magnetic effect [27], anomalous Hall effect [28, 29], discrete scale invariance [30], three-dimensional quantum Hall effect [31], exotic thermoelectric response [32–35], and photo-induced phase transition [36–40]. The understanding of the underlying electronic structure that drive these observations is of significant interest.

It has been pointed out that the electronic structure including the ground state topology are highly sensitive to the lattice constant of $ZrTe_5$ [1, 5] which in turn can be affected by the growth method [30, 41], consistent with experimental results showing the high sensitivity of the system to strain [42]. This calls for comprehensive studies of $ZrTe_5$ single crystals to connect observations of transport exotica with the electronic band structure. Here, we report an investigation of single crystals grown by chemical vapor transport (CVT) which are characterized by anomalously large and non-monotonic Seebeck and Nernst effects. We have further performed measurements of electronic transport, magnetic torque, and time and angle resolved photoemission spectroscopy (tr-ARPES) as well as electronic structure calculations. We show that we can quantitatively describe the thermoelectric, quantum oscillation, and spectroscopic results with a model of a small gap ($\Delta_{\text{gap}} = 27 \pm 5$ meV) TI with a temperature dependent Fermi level (shifting with rate $k_b \cdot \gamma = 0.48 \pm 0.06$ meV/K). This establishes a concrete description of $ZrTe_5$ grown in this manner that will further enable band engineering for topology and high thermoelectric performance.

II. RESULTS AND DISCUSSION

$ZrTe_5$ crystallizes in the orthorhombic structure of space group $Cmcm$ (D_{2h}^{17}, No.63), shown in Fig. 1(a, b). The structure is composed of $ZrTe_3$ prismatic chains oriented along the a-axis with additional Te atoms forming zig-zag between them. A weak inter-chain coupling exists such that two-dimensional layers are formed in the ac plane (denoted by black dashed lines). The coupling between the layers is van der Waals in nature and is much weaker than the inter-chain coupling; the crystal structure is highly anisotropic in all three directions. The crystals presented here were grown by chemical vapor transport [41] (CVT) and have a morphology character-

* Present Address: Lawrence Berkeley National Laboratory, Berkeley, California 94720, USA
† Present Address: Department of Physics, University of Illinois at Urbana-Champaign, Urbana, 61801 IL, USA
‡ Present Address: Department of Science, Toho University, Funabashi City, Chiba 274-8510, Japan

ized by a long ribbon-like shape with a typical dimension of 3 mm × 0.05 mm × 0.5 mm along the a, b, and c-axes.

A. Temperature dependence of Fermi level

We measured the electric and thermoelectric transport response in isothermal and open circuit conditions, respectively. A photo of the thermoelectric measurement setup is shown in Fig. 1(c). As shown in Fig. 1(d), the zero field longitudinal resistivity ρ_{xx} exhibits a hump structure upon cooling peaking near $T_p = 133$ K, as is often reported in CVT grown single crystals [22, 23, 25, 41, 43, 44]. Concomitant with this feature, the Seebeck coefficient S_{xx} passes through zero. The sign change of S_{xx}, as well as the low field Hall coefficient suggest that transport is dominated by hole type carriers for temperature $T > T_p$ and electron type below. For temperatures near T_p the zero field limit of slope of the Nernst effect $dS_{yx}/dB|_{B=0}$ shows a sign reversal. For $T < 80$ K, the system appears to cross over from semiconducting to Fermi liquid behavior suggestive of an electron-like metal. More quantitatively, a linear $S_{xx}(T)$ behavior typical for a normal metal is observed, following the Mott formula $S = \frac{\pi^2}{3}\frac{k_B^2 T}{e}\left(\frac{\partial \ln \sigma}{\partial \epsilon}\right)_{\epsilon_F}$, where ϵ_F is the Fermi level with respect to the band bottom and σ is electron conductivity. For a simple metal, this reduces to the well-known expression $S \propto \frac{k_B T}{\epsilon_F}$. A linear fit yields $\frac{dS_{xx}}{dT} = -1.59\ \mu\mathrm{V/K^2}$[45]. In addition, the electrical response is well described by parabolic law[46] $\rho_{xx} = \rho_0 + A \cdot T^2$, where $A = 0.05 \pm 0.02\ \mu\Omega \cdot \mathrm{cm/K^2}$. Qualitatively, this can be explained by a simple semiconducting band structure and T-dependent Fermi level as sketched Fig. 1(e).

We have performed angle-resolved photoemission spectroscopy (ARPES) on crystals from this same batch. Shown in Fig. 1(f) are energy-momentum cuts across the Γ point taken at $T = 35$ K and $T = 94$ K, as well as their difference. While the band shape remains largely unchanged, a clear downwards energy shifting at lower T is observed. Such a shift has been observed in a number of recent reports on CVT grown crystals [15, 16]. This is qualitatively consistent with the rigid band shift depicted in Fig. 1(e).

Significant attention has been aimed at understanding the nature of the band gap in $ZrTe_5$ including if it is gapped or gapless [15, 16], as well as the origin of resistivity anomaly [6–9]. We show here that the experimental observations above can be quantitatively captured by a gapped scenario depicted in Fig. 1(e). Starting with the assumption of a symmetric semiconducting band structure with a gap Δ_{gap} and Fermi level at ϵ_F, from the Drude model the low field Seebeck and Nernst coefficients are

$$S_{xx} = \frac{k_B}{e} \cdot \frac{pA^h - nA^e}{p+n}, \tag{1}$$

$$S_{yx} = \frac{k_B}{e} \cdot \frac{-2pn\left(A^h + A^e\right)}{(p+n)^2} \cdot \omega_c \tau_m \tag{2}$$

where k_B is Boltzmann constant, e is free electron charge, ω_c is the cyclotron frequency, τ_m is the momentum relaxation time, and $\frac{k_B}{e}A^{e(h)} = \frac{k_B}{e}\left(\frac{|\Delta\epsilon|}{k_B T} + 1\right)$ corresponds to the single carrier type Seebeck coefficient. Given the semiconducting structure, the electron (hole) density n (p) are proportional to $\exp(\frac{-|\Delta\epsilon|}{k_B T})$, with $|\Delta\epsilon|$ the energy difference between band top (bottom) and the Fermi level.

Previous ARPES observations suggest that the Fermi level shifting is approximately linear in energy in the intermediate T range of the resistivity anomaly [15]. We approximate $\epsilon_F - \epsilon_m \approx -\gamma k_B (T - T_m)$, where ϵ_m denotes the mid point of band gap, T_m denotes the temperature when Fermi level is degenerate with the midpoint, and γ is defined as a dimensionless shifting rate. Applying this to the model above, we arrive at expressions for the low field thermoelectric coefficients:

$$S_{xx} = \frac{k_B}{e} \cdot \left(\frac{\Delta_{\mathrm{gap}}}{2k_B T} + \frac{5}{2} - \beta\right) \cdot \tanh\left(\gamma \frac{T - T_m}{T}\right) - \frac{k_B}{e} \cdot \frac{\gamma(T - T_m)}{T}, \tag{3}$$

$$S_{yx} = \frac{-k_B}{e} \cdot \left(\frac{\Delta_{\mathrm{gap}}}{2k_B T} + \frac{5}{2} - \beta\right) \cdot \cosh^{-2}\left(\gamma \frac{T - T_m}{T}\right) \cdot \omega_c \tau_m, \tag{4}$$

$$\rho_{xx} = \frac{m^*}{(p+n)e^2\tau_m} \propto \frac{m^*}{e^2\tau_m} \cdot \exp\left(\frac{\Delta_{\mathrm{gap}}}{2k_B T}\right) \cdot \cosh^{-1}\left(\gamma \frac{T - T_m}{T}\right), \tag{5}$$

$$\rho_{yx} = \frac{B(p-n)}{e(p+n)^2} \propto \frac{B}{e} \cdot \exp\left(\frac{\Delta_{\mathrm{gap}}}{2k_B T}\right) \cdot \tanh\left(\gamma \frac{T - T_m}{T}\right) \cdot \cosh^{-1}\left(\gamma \frac{T - T_m}{T}\right) \tag{6}$$

Whereas a single-band semiconductor with a static Fermi level the thermoelectric coefficients will be monotonic and retain the same sign at different T, the shifting of ϵ_F allows for a dynamic response. The corresponding electrical response is also shown above. Similar to the case of the thermoelectric response, the additional degree of freedom associated with shifting ϵ_F makes an important modification to the electrical transport response as

a function of T.

We compare the expectations for Eq. (3)-(6) to the experimental results in Fig. 1(d). We directly fit $\rho_{xx}(T)$ and $S_{xx}(T)$ and for the Nernst and Hall response we fit the low field slope $\frac{dS_{yx}}{dB}\Big|_{B\to 0}$ and $\frac{d\rho_{yx}}{dB}\Big|_{B\to 0}$. The fit captures the intermediate and high T response with fit parameters and error bars listed in Table I. The obtained $k_b \cdot \gamma = 0.48 \pm 0.06$ meV/K is consistent with recent ARPES reports [15], where the band shifting rate is approximately 0.43 meV/K. The obtained $\Delta_{\rm gap} = 27 \pm 5$ meV is also consistent with our time-resolved ARPES, which we discuss below. The error bar above is defined as the standard deviation among the results in Table I.

For $T < 80$ K, the above model fails to capture the transport response, as would be expected upon entering the metallic regime. Moreover, as noted above, $\rho_{xx}(T)$ and $S_{xx}(T)$ are captured by the behavior of a simple metal, naturally suggestive of a drop in the magnitude of γ. However, the energy-momentum cut of the valence band from the present ARPES results suggests that band shifting persists below 94 K, which requires further theoretical attention.

B. Fermiology of conduction band

We further verify the above description of CVT grown $ZrTe_5$ by studying the Fermiology of the low temperaure band structure with quantum oscillations and tr-ARPES. For the former we examine the low temperature magnetoresistance $\Delta\rho_{xx}(H,T) \equiv \rho_{xx}(H,T) - \rho_{xx}(H,T = 15$ K), *i.e.* using the $T = 15$ K trace as a background. This is shown plotted against $1/H$ in Fig. 2(a) for field applied along the b axis. Clear Shubnikov-de Haas (SdH) oscillations are observed, onsetting near $\mu H_0 \sim 0.25$ T, indicating a quantum mobility exceeding $\mu = 1/\mu_0 H_0 \sim 4 \times 10^4$ cm^2/Vs. The oscillation frequency $B_f^{\hat{i}}$ is 5.070 ± 0.005 T which corresponds to a Fermi surface cross section $A_F^{ac} = 4.84 \pm 0.01 \times 10^{-4}$ Å^{-2}. This is consistent with de Haas-van Alphen oscillations observed in magnetic torque measurement[46].

We have measured the detailed angular dependence of the SdH effect; the variation of oscillation frequency $B_f^{\hat{i}}$ as the field rotates away from b axis are plotted in Fig. 2(e), where red squares (blue triangles) denotes rotating in ab (bc plane) and θ (ζ) denotes the angle between b axis and field direction. The angular variation is consistent with an ellipsoidal (3D) rather than cylindrical (quasi-2D) Fermi surface (dashed lines). This is also emphasized by the corresponding Landau fan diagrams (Fig. 2(e) inset) in which a saturating slope for $H\|b$ is observed. Assuming an ellipsoid Fermi surface, the corresponding Fermi wave vectors are $k_F^a = 9.46 \times 10^{-3}$ Å^{-1}, $k_F^c = 1.63 \times 10^{-2}$ Å^{-1} and $k_F^b = 9.32 \times 10^{-2}$ Å^{-1} (depicted in Fig. 2(d)). This ellipsoid Fermi pocket corresponds to a carrier density of $n = \frac{2}{(2\pi)^3} V_{FS} = 4.85 \times 10^{17}$ cm^{-3}, in good agreement with that obtained from the Hall coefficient $n = 4.71 \times 10^{17}$ cm^{-3}. Together, these provide a consistent picture of the low T Fermi surface being composed of a single electron pocket.

We can provide a further quantitative comparison with analysis of cyclotron effective mass m^*, carrier lifetime τ, and effective g factor from the Lifshitz-Kosevich formula [47]:

$$\Delta\rho_{xx} \propto R_T R_D R_S \cdot \cos\left(2\pi(\frac{B_f^{\hat{i}}}{B} + \phi)\right) \tag{7}$$

The oscillation amplitude is modulated by three factors: the thermal factor $R_T = \frac{\alpha T}{B}/\sinh(\frac{\alpha T}{B})$ due to thermal broadening, the Dingle factor $R_D = \exp\left(\frac{-\alpha T_D}{B}\right)$ due to scattering, and the spin factor $R_S = \cos\left(\frac{\pi g m^*}{2m_e}\right)$ due to Zeeman splitting, where $\alpha = \frac{2\pi^2 k_B m^*}{e\hbar}$. The oscillation amplitude $\Delta\rho_{xx}(T)$ at fixed field ($H\|b$) is plotted in Fig. 2(b), with a fit to R_T yielding an average ac-plane $m_{ac}^* = 0.028 m_e$ (the result of each field is shown inset) and Fermi velocity $v_F^{ac} = \hbar\langle k_F^{ac}\rangle/m_{ac}^* = 4.1 \times 10^5$ m/s. As shown in Fig. 2(c), an average Dingle temperature $T_D = 1.65$ K is found from a linear fit to $\ln(\Delta\rho_{xx}/R_T)/\alpha \propto \ln(R_D)/\alpha = \frac{-T_D}{B}$. From $T_D = \frac{\hbar}{2\pi k_B \tau}$ this corresponds to a lifetime $\tau = 0.75$ ps, comparable to $\tau_m = 1.17$ ps calculated from the Hall mobility and m_{ac}^*.

We note that the analysis of above is restricted to $\mu_0 H < 1.3$ T, as in larger field a pronounced Zeeman splitting becomes evident, as shown in Fig. 2(a) and its inset. The modulation effect due to R_S can be rewritten as

$$R_S \cos\left(2\pi(\frac{B_f}{B} + \phi)\right) = \frac{1}{2}\sum_{\uparrow,\downarrow} \cos\left(2\pi(\frac{B_f^{\uparrow(\downarrow)}}{B} + \phi \pm \frac{g m^*}{4m_e})\right) \tag{8}$$

where the summation is over two spins (+(-) for spin up $\uparrow$ (down $\downarrow$)). Therefore, the spin split Landau level indeces correspond to the lines with $n_{\uparrow(\downarrow)} = \frac{B_f^{\uparrow(\downarrow)}}{B} + \phi \pm \frac{g m^*}{4m_e}$, as shown in the inset of Fig. 2(a) for $H\|b$. Linear fitting gives $B_f^{\uparrow} = 4.85 \pm 0.04$ T (intercept$=0.29 \pm 0.02$) and $B_f^{\downarrow} = 5.31 \pm 0.07$ T (intercept$=-0.16 \pm 0.04$), corresponding to $g \approx 25.8$.

Turning to spectroscopy of the conduction band, results of tr-ARPES performed at $T = 35$ K are shown in Fig. 3(a, b). Here, the conduction band at ϵ_F and the band gap $\Delta_{\rm gap}$ are clearly resolved. The horizontal red bar and dashed red lines in Fig. 3(a) indicate the magnitude of Fermi wave vector k_F^a and Fermi velocity v_F^{ac} obtained from quantum oscillations, which are in approximate agreement. $\Delta_{\rm gap}$ derived from the transport data in Fig. 1(d) is also drawn in Fig. 3(a). In Fig. 3(b) the Fermi surface cross section is again compared with an in-plane spectrum, showing good agreement at ϵ_F.

Using the Brillion zone defined in Fig. 3(c), in Fig. 3(d) we show the band structure at Γ point of the three possible phases for $ZrTe_5$, namely strong TI (left panel),

TABLE I. Comparison of fitting parameters for the Fermi level shifting rate γ, zero-field energy gap $\Delta_{\rm gap}$, mid-point temperature T_m, and power law of inverse scattering time τ for three samples s0, s1, and s2. Fitting to the zero field resistivity ρ_{xx}, low field slope of the Nernst response dS_{yx}/dB, zero field Seebeck coefficient S_{xx}, and low field Hall slope $d\rho_{yx}/dB$ are shown.

sample	s0	s1	s1	s2	s2
Fitting	$\rho_{xx}(B=0)$	$(dS_{yx}/dB)_{B\to 0}$	$S_{xx}(B=0)$	$\rho_{xx}(B=0)$	$(d\rho_{yx}/dB)_{B\to 0}$
Fit regime	110-190 K	100-300 K	80-300 K	110-190 K	100-180 K
$k_b\cdot\gamma$ (meV/K)	0.42 ± 0.01	0.55 ± 0.02	0.53 ± 0.02	0.417 ± 0.004	0.46 ± 0.03
$\Delta_{\rm gap}$ (meV)	25 ± 27	-	24 ± 2	33 ± 8	-
T_m (K)	136.6 ± 0.9	130 ± 2	137.0 ± 0.4	142.1 ± 0.2	127 ± 1
β ($\tau\propto T^{-\beta}$)	1.8 ± 1.0	0.2 ± 1.1	1.00 ± 0.08	1.7 ± 0.3	-

Dirac semimetal (middle), and weak TI (right), calculated by density functional theory (DFT) [46, 48–53]. The electronic topology of $ZrTe_5$ is known to be extremely sensitive to the values of its lattice constants [5]; here, the three panels in Fig. 3(d) are obtained in series through expanding unit cell volume by 8×10^{-7}%, from left to right (the direct gap for the strong TI and weak TI phase nominally agree with experimental observations). In each, the Fermi level is shown for which the Fermi surface volume matches that of the quantum oscillation analysis (dashed line). The corresponding Fermi pockets are plotted in the insets. The band inversion of the strong TI leads to a weaker dispersion; comparing the flatness of these ellipsoids, the strong TI case is closer to that from quantum oscillation results depicted in Fig. 2(d). However, surface states were not seen in the tr-ARPES measurements (nor in the previous static ARPES reports with high energy resolution [15, 16]), which indicates an weak TI. Nevertheless, one possible scenario for this within a strong TI system is leakage of surface state into the bulk due to small band gap. The expected inelastic mean free path of excited electrons here is 2-7 nm compared to the penetration depth of surface states estimated to be 45 nm from $\Delta_{\rm gap}=\frac{(\hbar k)^2}{2m^*}$. Additional experiments to probe the potential surface states are of significant interest.

C. Field Enhancement of S_{xx} and S_{yx}

At 100 K $< T <$ 150 K where the thermoelectric response changes most rapidly, we observe a strong enhancement of both S_{xx} and S_{yx} with increasing $H\|b$, consistent with recent report [32, 35]. As shown in Fig. 4(a, b), peak magnitude of $S_{xx}(T)$ is enhanced more than 3 fold at 14 T, reaching 500 μV/K, while that of S_{yx} approaches 700 μV/K. The maximum values at fixed H for both quantities appear to be monotonically increasing with H without saturation at our largest applied fields (see Fig. 4(d)). The Seebeck coefficient of a simple metal is not typically strongly enhanced in field; this suggests a significant modification to the electronic band structure. Given the acute sensitivity of ϵ_F to T, one natural origin for this response would be a magnetic field dependence to ϵ_F. To connect these, we plot the H dependence of the T at which the thermoelectric coefficients peaked and the zero crossing for $S_{xx}(T)$ occur. They show similar behavior with features shifting towards higher temperature for stronger magnetic fields, consistent with a spin down valence band being raised by the Zeeman energy at high temperature. Upon cooling, this would lead to the Fermi level traversing the gap at higher T, which can be tracked by a vanishing $S_{xx}(T)$ and maximal $S_{yx}(T)$. From zero field to $H=14$ T, the observed shift is approximately 40 K, which corresponds to a Fermi level shift of ≈ 20 meV given the fitted shift rate γ from Table I. This is comparable to the size of the Zeeman splitting ≈ 20 meV given the large g factor. We note also this is approaching the size of the zero-field energy gap, suggesting a potentially complex evolution at high field. Thus despite their unusually large magnitude, these effects are consistent with the band structure described above. It is of significant interest to pursue these and related materials to higher magnetic fields to test recent predictions for extremely large field-induced figure of merit ZT in systems with highly dispersive bands [54].

III. CONCLUSION

We have synthesized single crystals of $ZrTe_5$ by chemical vapor transport and probed the band properties via electric and thermoelectric transport, magnetic torque, and tr-ARPES. Both transport and photoemission results indicate a temperature dependent Fermi level shifting across a small gap. A semiclassical calculation of the transport coefficients based on such a model describes the observations, yielding $k_b\cdot\gamma = 0.48\pm0.06$ mev/K and $\Delta_{\rm gap} = 27\pm5$ meV. For T below this range, the system behaves metallically. Quantum oscillations and ARPES reveal a consistent picture of an a light-mass ($0.028m_e$), small ellipsoidal electron pocket with large $v_F\approx 4\times10^5$ m/s. First principle calculations of band structures for each topological phase are done to compare with quantum oscillation results. The lack of surface states in ARPES is consistent with weak TI regime, whereas they may also be explained by the leakage of

surface state into the bulk due to the small band gap. Finally, a significant enhancement of both the Seebeck and Nernst effect with magnetic field indicates that the band structure is strongly affected in H, consistent with the relatively large $g = 25.8$. Together this study demonstrates that comprehensive experiments and analysis of single crystals of $ZrTe_5$ grown in the same manner can produce a clear picture of the underlying physical mechanisms for unusual transport effects. Extending these studies to the recent exotica reported [27–31, 33, 36–40] in $ZrTe_5$ grown by various methods may elucidate the origin of the rich electronic physics in this system.

IV. ACKNOWLEDGEMENTS

This work was supported primarily by the U.S. Department of Energy, Office of Science, Basic Energy Sciences, under Award Number DE-SC0020149 (electrical measurements, tr-ARPES, and analysis) and also by the Gordon and Betty Moore Foundations EPiQS Initiative, Grant GBMF9070 to J.G.C. (materials synthesis and DFT calculations).

[1] H. Weng, X. Dai, and Z. Fang, Phys. Rev. X **4**, 011002 (2014).
[2] S. Okada, T. Sambongi, and M. Ido, Journal of the Physical Society of Japan **49**, 839 (1980).
[3] S. Okada, T. Sambongi, M. Ido, Y. Tazuke, R. Aoki, and O. Fujita, Journal of the Physical Society of Japan **51**, 460 (1982), https://doi.org/10.1143/JPSJ.51.460.
[4] T. Jones, W. Fuller, T. Wieting, and F. Levy, Solid State Communications **42**, 793 (1982).
[5] Z. Fan, Q.-F. Liang, Y. Chen, S.-H. Yao, and J. Zhou, Scientific reports **7**, 45667 (2017).
[6] B. Fu, H.-W. Wang, and S.-Q. Shen, Physical Review Letters **125**, 256601 (2020).
[7] C. Wang, Physical Review Letters **126**, 126601 (2021).
[8] B. Monserratand A. Narayan, Physical Review Research **1**, 033181 (2019).
[9] N. Aryal, X. Jin, Q. Li, A. M. Tsvelik, and W. Yin, Physical Review Letters **126**, 016401 (2021).
[10] G. Manzoni, A. Sterzi, A. Crepaldi, M. Diego, F. Cilento, M. Zacchigna, P. Bugnon, H. Berger, A. Magrez, M. Grioni, and F. Parmigiani, Phys. Rev. Lett. **115**, 207402 (2015).
[11] L. Moreschini, J. C. Johannsen, H. Berger, J. Denlinger, C. Jozwiak, E. Rotenberg, K. S. Kim, A. Bostwick, and M. Grioni, Phys. Rev. B **94**, 081101 (2016).
[12] R. Wu, J.-Z. Ma, S.-M. Nie, L.-X. Zhao, X. Huang, J.-X. Yin, B.-B. Fu, P. Richard, G.-F. Chen, Z. Fang, X. Dai, H.-M. Weng, T. Qian, H. Ding, and S. H. Pan, Phys. Rev. X **6**, 021017 (2016).
[13] G. Manzoni, L. Gragnaniello, G. Autès, T. Kuhn, A. Sterzi, F. Cilento, M. Zacchigna, V. Enenkel, I. Vobornik, L. Barba, F. Bisti, P. Bugnon, A. Magrez, V. N. Strocov, H. Berger, O. V. Yazyev, M. Fonin, F. Parmigiani, and A. Crepaldi, Phys. Rev. Lett. **117**, 237601 (2016).
[14] G. Manzoni, A. Crepaldi, G. Autès, A. Sterzi, F. Cilento, A. Akrap, I. Vobornik, L. Gragnaniello, P. Bugnon, M. Fonin, *et al.*, Journal of Electron Spectroscopy and Related Phenomena **219**, 9 (2017).
[15] Y. Zhang, C. Wang, L. Yu, G. Liu, A. Liang, J. Huang, S. Nie, X. Sun, Y. Zhang, B. Shen, *et al.*, Nature communications **8**, 15512 (2017).
[16] H. Xiong, J. A. Sobota, S.-L. Yang, H. Soifer, A. Gauthier, M.-H. Lu, Y.-Y. Lv, S.-H. Yao, D. Lu, M. Hashimoto, P. S. Kirchmann, Y.-F. Chen, and Z.-X. Shen, Phys. Rev. B **95**, 195119 (2017).
[17] X.-B. Li, W.-K. Huang, Y.-Y. Lv, K.-W. Zhang, C.-L. Yang, B.-B. Zhang, Y. B. Chen, S.-H. Yao, J. Zhou, M.-H. Lu, L. Sheng, S.-C. Li, J.-F. Jia, Q.-K. Xue, Y.-F. Chen, and D.-Y. Xing, Phys. Rev. Lett. **116**, 176803 (2016).
[18] R. Y. Chen, S. J. Zhang, J. A. Schneeloch, C. Zhang, Q. Li, G. D. Gu, and N. L. Wang, Phys. Rev. B **92**, 075107 (2015).
[19] R. Y. Chen, Z. G. Chen, X.-Y. Song, J. A. Schneeloch, G. D. Gu, F. Wang, and N. L. Wang, Phys. Rev. Lett. **115**, 176404 (2015).
[20] Y. Jiang, Z. L. Dun, H. D. Zhou, Z. Lu, K.-W. Chen, S. Moon, T. Besara, T. M. Siegrist, R. E. Baumbach, D. Smirnov, and Z. Jiang, Phys. Rev. B **96**, 041101 (2017).
[21] Z.-G. Chen, R. Y. Chen, R. D. Zhong, J. Schneeloch, C. Zhang, Y. Huang, F. Qu, R. Yu, Q. Li, G. D. Gu, and N. L. Wang, Proceedings of the National Academy of Sciences **114**, 816 (2017), https://www.pnas.org/content/114/5/816.full.pdf.
[22] G. Zheng, J. Lu, X. Zhu, W. Ning, Y. Han, H. Zhang, J. Zhang, C. Xi, J. Yang, H. Du, K. Yang, Y. Zhang, and M. Tian, Phys. Rev. B **93**, 115414 (2016).
[23] Y. Liu, X. Yuan, C. Zhang, Z. Jin, A. Narayan, C. Luo, Z. Chen, L. Yang, J. Zou, X. Wu, *et al.*, Nature communications **7**, 12516 (2016).
[24] G. Zheng, X. Zhu, Y. Liu, J. Lu, W. Ning, H. Zhang, W. Gao, Y. Han, J. Yang, H. Du, K. Yang, Y. Zhang, and M. Tian, Phys. Rev. B **96**, 121401 (2017).
[25] J. L. Zhang, C. Y. Guo, X. D. Zhu, L. Ma, G. L. Zheng, Y. Q. Wang, L. Pi, Y. Chen, H. Q. Yuan, and M. L. Tian, Phys. Rev. Lett. **118**, 206601 (2017).
[26] Y.-Y. Lv, B.-B. Zhang, X. Li, K.-W. Zhang, X.-B. Li, S.-H. Yao, Y. B. Chen, J. Zhou, S.-T. Zhang, M.-H. Lu, S.-C. Li, and Y.-F. Chen, Phys. Rev. B **97**, 115137 (2018).
[27] Q. Li, D. E. Kharzeev, C. Zhang, Y. Huang, I. Pletikosić, A. Fedorov, R. Zhong, J. Schneeloch, G. Gu, and T. Valla, Nature Physics **12**, 550 (2016).
[28] T. Liang, J. Lin, Q. Gibson, S. Kushwaha, M. Liu, W. Wang, H. Xiong, J. A. Sobota, M. Hashimoto, P. S. Kirchmann, *et al.*, Nature Physics **14**, 451 (2018).
[29] P. M. Lozano, G. Cardoso, N. Aryal, D. Nevola, G. Gu, A. Tsvelik, W. Yin, and Q. Li, arXiv preprint arXiv:2112.15227 (2021).
[30] H. Wang, H. Liu, Y. Li, Y. Liu, J. Wang, J. Liu, J.-Y. Dai, Y. Wang, L. Li, J. Yan, *et al.*, Science advances **4**,

eaau5096 (2018).
[31] F. Tang, Y. Ren, P. Wang, R. Zhong, J. Schneeloch, S. A. Yang, K. Yang, P. A. Lee, G. Gu, Z. Qiao, *et al.*, Nature **569**, 537 (2019).
[32] J. Zhang, C. Wang, C. Guo, X. Zhu, Y. Zhang, J. Yang, Y. Wang, Z. Qu, L. Pi, H.-Z. Lu, *et al.*, Physical review letters **123**, 196602 (2019).
[33] W. Zhang, P. Wang, B. Skinner, R. Bi, V. Kozii, C.-W. Cho, R. Zhong, J. Schneeloch, D. Yu, G. Gu, *et al.*, Nature communications **11**, 1 (2020).
[34] W. Zhang, P. Wang, G. Gu, X. Wu, and L. Zhang, Physical Review B **102**, 115147 (2020).
[35] P. Wang, C.-w. Cho, F. Tang, P. Wang, W. Zhang, M. He, G. Gu, X. Wu, Y. Shao, and L. Zhang, Physical Review B **103**, 045203 (2021).
[36] C. Vaswani, L.-L. Wang, D. H. Mudiyanselage, Q. Li, P. M. Lozano, G. D. Gu, D. Cheng, B. Song, L. Luo, R. H. J. Kim, C. Huang, Z. Liu, M. Mootz, I. E. Perakis, Y. Yao, K. M. Ho, and J. Wang, Phys. Rev. X **10**, 021013 (2020).
[37] T. Konstantinova, L. Wu, W.-G. Yin, J. Tao, G. Gu, X. Wang, J. Yang, I. Zaliznyak, and Y. Zhu, npj Quantum Materials **5**, 1 (2020).
[38] L. Luo, D. Cheng, B. Song, L.-L. Wang, C. Vaswani, P. Lozano, G. Gu, C. Huang, R. H. Kim, Z. Liu, *et al.*, Nature Materials **20**, 329 (2021).
[39] N. Aryal, X. Jin, Q. Li, M. Liu, A. Tsvelik, and W. Yin, npj Computational Materials **8**, 1 (2022).
[40] L.-L. Wang, Physical Review B **103**, 075105 (2021).
[41] Y.-Y. Lv, F. Zhang, B.-B. Zhang, B. Pang, S.-H. Yao, Y. Chen, L. Ye, J. Zhou, S.-T. Zhang, and Y.-F. Chen, Journal of Crystal Growth **457**, 250 (2017).
[42] J. Mutch, W.-C. Chen, P. Went, T. Qian, I. Z. Wilson, A. Andreev, C.-C. Chen, and J.-H. Chu, Science advances **5**, eaav9771 (2019).
[43] D. McIlroy, S. Moore, D. Zhang, J. Wharton, B. Kempton, R. Littleton, M. Wilson, T. Tritt, and C. Olson, Journal of Physics: Condensed Matter **16**, L359 (2004).
[44] Y. Zhou, J. Wu, W. Ning, N. Li, Y. Du, X. Chen, R. Zhang, Z. Chi, X. Wang, X. Zhu, P. Lu, C. Ji, X. Wan, Z. Yang, J. Sun, W. Yang, M. Tian, Y. Zhang, and H.-k. Mao, Proceedings of the National Academy of Sciences **113**, 2904 (2016), https://www.pnas.org/content/113/11/2904.full.pdf.
[45] J. M. Ziman, *Electrons and phonons: the theory of transport phenomena in solids* (Oxford university press, 2001).
[46] See Supplementary Materials.
[47] D. Shoenberg, *Magnetic Oscillations in Metals*, Arnold and Caroline Rose Monograph Series of the American So (Cambridge University Press, 1984).
[48] G. Kresseand J. Furthmüller, Phys. Rev. B **54**, 11169 (1996).
[49] G. Kresseand J. Furthmüller, Comput. Mater. Sci. **6**, 15 (1996).
[50] P. E. Blöchl, Phys. Rev. B **50**, 17953 (1994).
[51] J. P. Perdew, K. Burke, and M. Ernzerhof, Phys. Rev. Lett. **77**, 3865 (1996).
[52] H. J. Monkhorstand J. D. Pack, Phys. Rev. B **13**, 5188 (1976).
[53] L. Fuand C. L. Kane, Phys. Rev. B **76**, 045302 (2007).
[54] B. Skinnerand L. Fu, Science advances **4**, eaat2621 (2018).

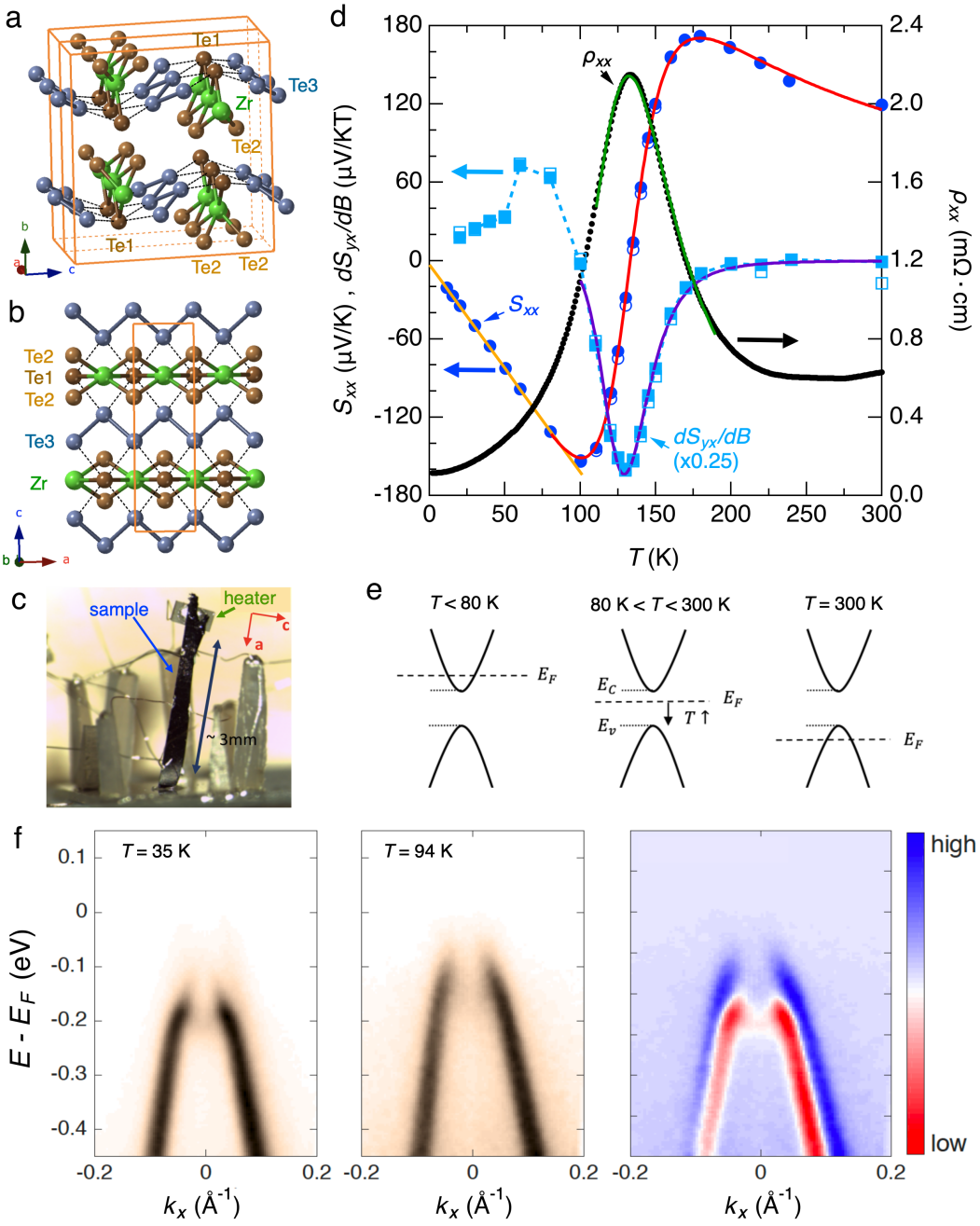

FIG. 1. (a,b) Crystal structure of layered compound $ZrTe_5$. (c) Photo of thermoelectric measurement setup. (d) Resistivity and thermoelectric response for the zero magnetic field limit. The solid and open blue circles (cyan squares) of S_{xx} (S_{yx}) refer to data with heater power 0.25 mW and 0.5 mW. Solid lines in (d) are fittings according to the Fermi level shifting model sketched in (e) (see text). (f) ARPES energy-momentum cuts across the Γ point taken at temperatures of 35 K (left) and 94 K (middle); darker color denotes higher intensity. The intensity difference (high temperature minus low temperature) is shown in the rightmost panel.

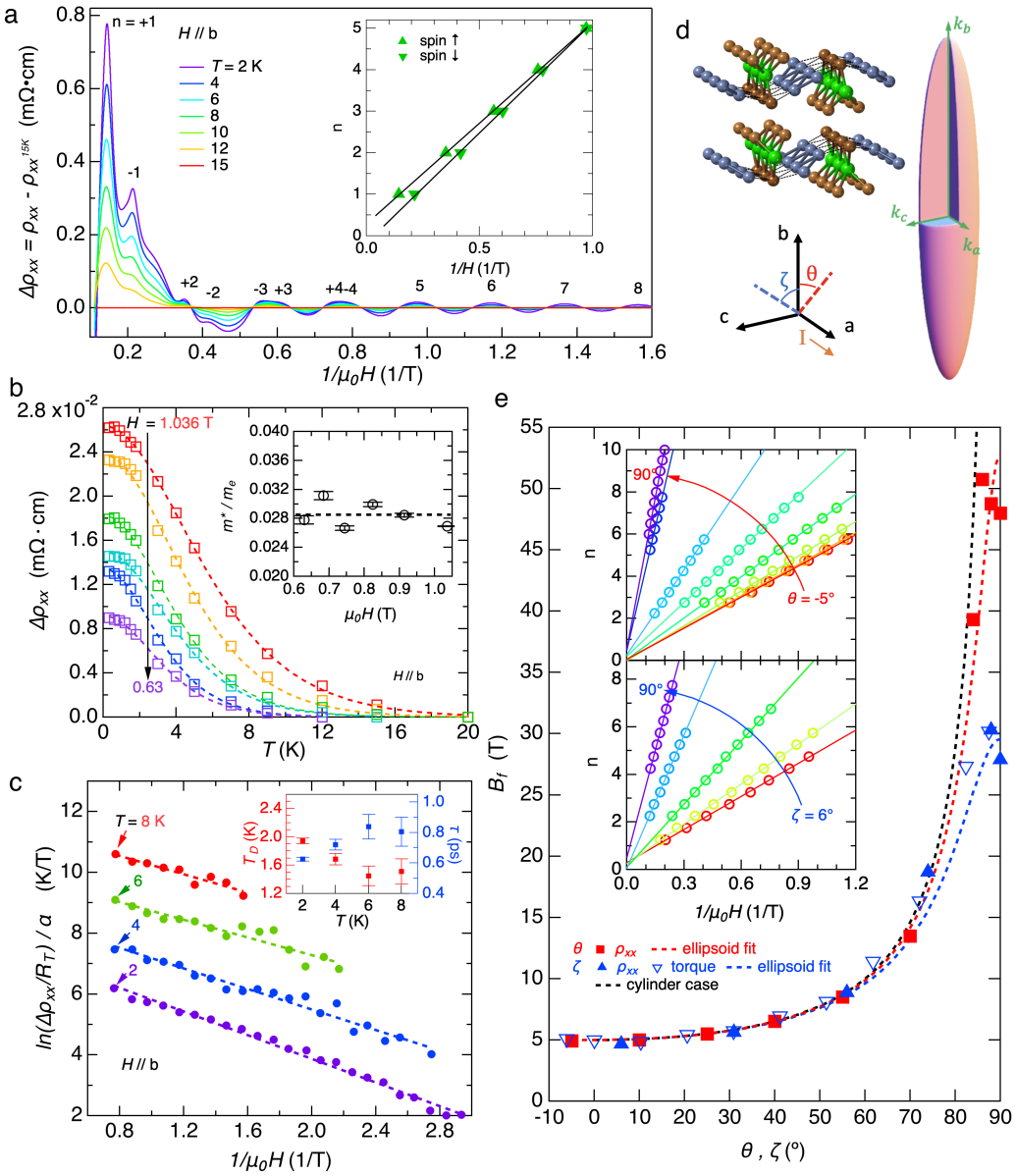

FIG. 2. (a) Oscillatory magnetoresistance $\Delta\rho_{xx} \equiv \rho_{xx}(H,T) - \rho_{xx}(H,T = 15\ \mathrm{K})$. The inset shows the spin-split Landau fan diagram. (b) Oscillation amplitude $\Delta\rho_{xx}$(T) at fixed field with $H\|b$. Dashed lines are fittings according to thermal damping (see text) and the fitted effective mass is plotted in the inset. (c) Dingle analysis fits, where $\alpha = \frac{2\pi^2 k_B m^*}{\hbar e}$. The fitted Dingle temperature T_D and carrier lifetime τ are plotted in the inset. (d) Illustration of measurement configuration for quantum oscillations and relation to crystal structure along with a schematic depiction of the observed ellipsoidal Fermi surface. (e) Quantum oscillation frequency as a function of field angle. Red squares (blue triangles) refer to rotating from b to a (c) axis. Both transport (solid) and torque (open) results are plotted. Dashed lines are fits to either ellipsoid or cylinder Fermi surface. Landau fan diagrams are shown in the insets.

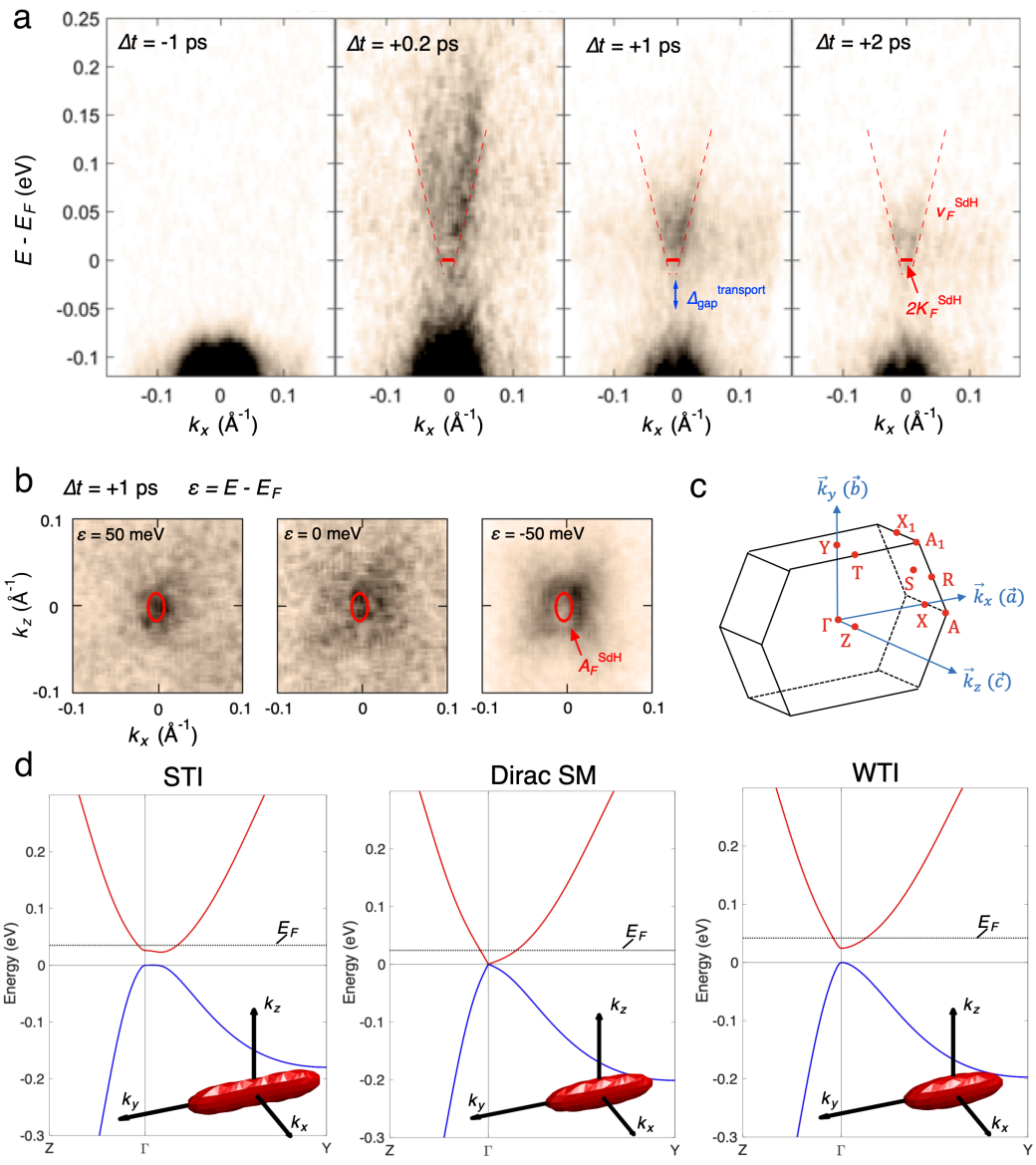

FIG. 3. (a) tr-ARPES energy-momentum cuts across the Γ point at different time delays, probed at $T = 35$ K. k_x is along the a-axis and $k_x = 0$ corresponds to the Γ point. At the Fermi level, the solid red bar and dashed line refer to k_F^a and v_F^{ac} determined from quantum oscillations, respectively. The gap size $\Delta_{\rm gap}$ is determined from the transport data analysis is also drawn. (b) Energy contours obtained 1 ps after photoexcitation, at energy $\epsilon = E - E_F = 50$, 0, -50 meV, where k_x is along the a axis and k_z is along the c axis. The integration window is 50 meV. The red ellipse represents the Fermi surface size obtained from quantum oscillations. (c) Brillioun zone and (d) band structure calculated by density functional theory. The left, middle and right panels correspond to strong topological insulator (TI), Dirac semimetal (SM) and weak TI phases, respectively. For each scenario, the low temperature Fermi level is denoted by the dashed line, determined by the Fermi surface volume from quantum oscillations. The corresponding Fermi pocket is depicted in the inset.

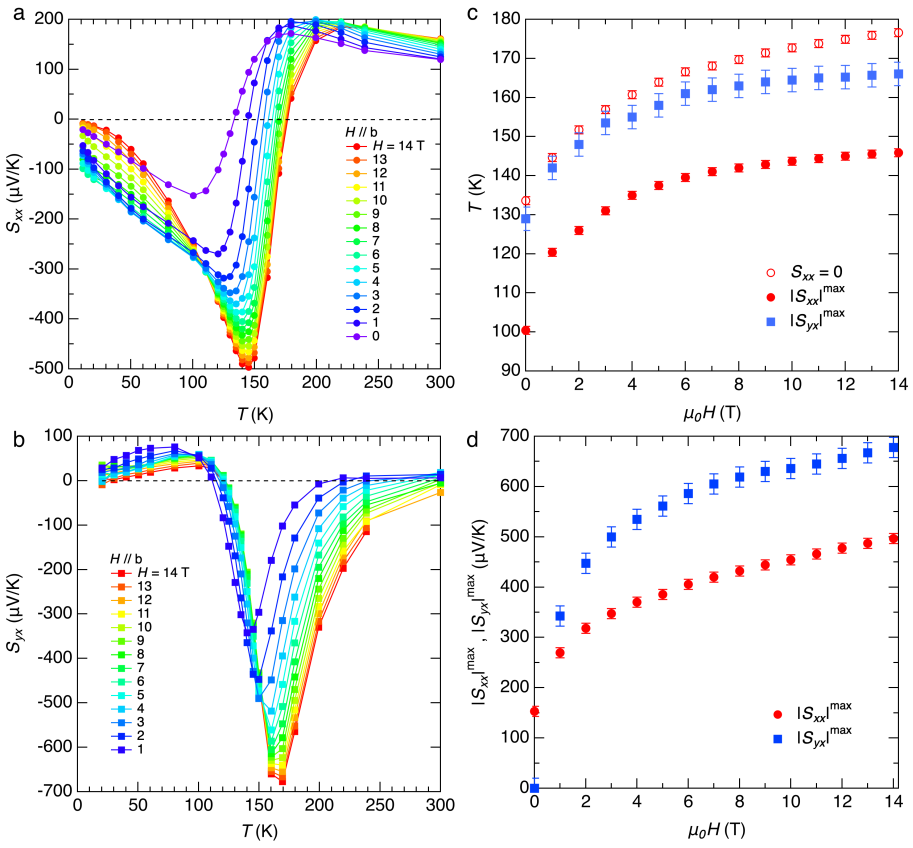

FIG. 4. (a) Thermopower S_{xx} and (b) Nernst coefficient S_{yx} as a function of temperature in different magnetic field H. (c) Shifting of the S_{xx} and S_{yx} peak temperature with H as well as the H-dependence of the zero-crossing of $S_{xx}(T)$. (d) The maximum value of S_{xx} and S_{yx} as a function of magnetic field. The error bars in (c) and (d) reflect the discreteness of the field-dependent data set.